# Shape-memory polymer metamaterials based on triply periodic minimal surfaces

Roudbarian, Nima; Jebellat, Ehsan; Famouri, Seyedfarzad; Baniasadi, Mahdi; Hedayati, Reza; Baghani, Mostafa

**DOI**
10.1016/j.euromechsol.2022.104676

**Publication date**
2022

**Document Version**
Final published version

**Published in**
European Journal of Mechanics, A/Solids

**Citation (APA)**
Roudbarian, N., Jebellat, E., Famouri, S., Baniasadi, M., Hedayati, R., & Baghani, M. (2022). Shape-memory polymer metamaterials based on triply periodic minimal surfaces. *European Journal of Mechanics, A/Solids*, *96*, Article 104676. https://doi.org/10.1016/j.euromechsol.2022.104676

European Journal of Mechanics / A Solids 96 (2022) 104676

Contents lists available at ScienceDirect

European Journal of Mechanics / A Solids

journal homepage: www.elsevier.com/locate/ejmsol

# Shape-memory polymer metamaterials based on triply periodic minimal surfaces

Nima Roudbarian [a], Ehsan Jebellat [b], Seyedfarzad Famouri [c], Mahdi Baniasadi [a], Reza Hedayati [d,**], Mostafa Baghani [a,*]

[a] School of Mechanical Engineering, College of Engineering, University of Tehran, Tehran, Iran
[b] Department of Mechanical Engineering, Colorado School of Mines, Golden, CO, 80401, USA
[c] The Robotic Surgery Lab, Mechanical Engineering Department, Concordia University, Montreal, QC, Canada
[d] Department of Aerospace Structures and Materials (ASM), Faculty of Aerospace Engineering, Delft University of Technology (TU Delft), Delft, Netherlands

A R T I C L E I N F O

*Keywords:*
Smart materials
Shape-memory polymers
Metamaterials
Triply periodic minimal surfaces
Self-fitting
Finite element analysis

A B S T R A C T

Triply periodic minimal surfaces (TPMS) metamaterials and shape-memory polymer (SMP) smart materials are known for their beneficial attributes in novel scientific and industrial fields. Through TPMS designs, low weight accompanied by high surface area are achievable, which are known as crucial parameters in many fields, such as tissue engineering. Moreover, SMPs are well-suited to generate force or to recover their permanent shape by means of an external stimulus. Combining these properties is possible by fabricating TPMS-based metamaterials made out of SMPs, which can be applicable in numerous applications. By considering different level volume fraction of four types of TPMS-based lattices (diamond, gyroid, IWP, and primitive), we focus on the effect of micro-architecture on shape-memory characteristics (i.e., shape recovery, shape fixity, and force recovery) as well as mechanical properties (elastic modulus and Poisson's ratio) of these smart metamaterials. For this purpose, shape-memory effect (SME) is simulated employing thermo-visco-hyperelastic constitutive equations coupled with the time-temperature superposition principle. It is observed that by increasing the level volume fraction of each lattice type, the elastic modulus, shape fixity, and force recovery increase, while the shape recovery diminishes. Such behaviors can be attributed to different deformation modes (flexural or uniaxial) in SMP TPMS-based metamaterials. Furthermore, it is shown that the Poisson's ratio has a nonlinear behavior in these structures. The smart metamaterials introduced in this study have the advantage of providing the possibility of designing implants, especially in bone defects tailored with different micro-architectures depending on each patient's specific need.

## 1. Introduction

Due to recent exponential technological advances in science and industry, a new group of systems known as smart systems has emerged. Such systems usually require responsive smart elements such as smart sensors and actuators, which are in many cases made out of smart materials. Smart Materials can reform from their temporary shape to their original one in response to an external stimulus such as temperature, light, magnetic field, electrical potential, and pH (Janbaz et al., 2016; Abdolahi et al., 2017; Roudbarian et al., 2019a). These materials have myriad applications in different fields, such as aerospace engineering (Liu et al., 2014), robotics (Jebellat et al., 2021; Jin et al., 2018), textile engineering (Zhang et al., 2018; Udhayaraman and Mulay, 2019), medical devices (Zhao et al., 2019; Sadipour et al., 2020), drug delivery (Gharehnazifam et al., 2021, 2022; Bayat et al., 2020), and biomaterials (Janbaz et al., 2016; Asadzadeh et al., 2020). Among them, shape-memory polymer (SMP) is a type of smart material that can intake shape-memory effect (SME). To improve the SME, as there are a wide range of influential parameters in SMP behavior, these materials can be examined from various aspects, such as geometric and structural design (Jebellat et al., 2020; Roudbarian et al., 2019b), constitutive modeling (Yarali et al., 2020a; Lotfolahpour and Zaeem, 2021), addition of nano-particles (Abbasi-Shirsavar et al., 2019; Magnusson et al., 2022), and macromolecular details (Ghaderi et al., 2020). SMPs or their

---

* Corresponding author.
** Corresponding author.
*E-mail addresses:* rezahedayati@gmail.com, r.hedayati@tudelft.nl (R. Hedayati), baghani@ut.ac.ir (M. Baghani).

https://doi.org/10.1016/j.euromechsol.2022.104676
Received 22 October 2021; Received in revised form 19 May 2022; Accepted 27 May 2022

composites (Moshki et al., 2022; Roudbarian et al., 2021) have been considered in recent years as one of the main classes of shape-memory materials. Although SMPs, as compared to shape-memory alloys, usually generate much smaller force levels and possess lower strengths, they have many advantages including low cost, low density, low energy consumption for shape programming, ability of large elastic deformation, excellent manufacturability, biocompatibility, and biodegradability (Baghani et al., 2012; Damanpack et al., 2015).

Metamaterials, a spotlight of researchers nowadays, are special types of designer materials having unusual mechanical properties and advanced functionalities usually not found in nature (Kolken and Zadpoor, 2017). The term "metamaterial" was firstly used in optics and electromagnetism fields (Smith et al., 2004; Shalaev, 2007); however, they have found their way into mechanical aspects of materials, and therefore, a new branch called "mechanical metamaterials" has emerged. On the contrary to conventional materials, mechanical metamaterials can exhibit properties such as negative Poisson's ratio (NPR) (Ghavidelnia et al., 2020; Jebellat et al., 2020), negative elasticity (Liu et al., 2011), negative compressibility (Zadpoor, 2016), and fluid-like behavior (Mohammadi et al., 2020), and photonic lattices (Ko et al., 2021). To achieve these special mechanical and physical properties, repeatable micro-structural topologies should be designed in nano- and micro-scales. By recent developments in additive manufacturing (AM) technologies, fabricating complicated structures in the noted scales has become possible (Akbari et al., 2201). This matter has attracted many manufacturers and scientists to the field of mechanical metamaterials (Zadpoor, 2016; Noroozi et al., 2020). Therefore, studying the relation between the topology in micro- and macro-scale properties in all mechanical materials seems to be indisputable.

There are a few well-known strut-based open-cell lattice structures, such as rhombic dodecahedron (Hedayati et al., 2018), truncated octahedron (Qi et al., 2019), BCC (Ptochos and Labeas, 2012), truncated cube (Hedayati et al., 2016), etc. However, strut-based lattice structures have the disadvantage of having low surface area to volume fraction ratio and relatively low curvature in their internal surfaces, which are both crucial parameters in applications including tissue regeneration (Bobbert et al., 2017). Nature has resolved the problem of low weight accompanied by high surface area and curvature with creating specific micro-geometries known as triply minimally periodic surface (TPMS). TPMS structures can be found in butterfly wings (Pouya et al., 2016), sea urchin (Lai et al., 2007), block copolymers (Matsen and Bates, 1996), and soap films (Schoen, 1970). The unit cells inspired by the noted natural structures, which are also the most favorable structures among the researchers in the field (Soyarslan et al., 2019; du Plessis et al., 2020; Abueidda et al., 2017), will be implemented in this study for constructing shape-memory TPMS-based metamaterials (Fig. 1).

For the first time, Schwarz (1890) implemented nature-based TPMS diamond and primitive topologies in 1865. Despite the great benefits they offer, it was not possible to create intricate TPMS structures fast and accurately in the 20th century due to limitations in manufacturing. With recent advances in AM, many new TPMS microstructures, such as gyroid (du Plessis et al., 2020), primitive (Yin et al., 2021), diamond (Maszybrocka et al., 2019), IWP (Abueidda et al., 2017), Neovius-CM (Abueidda et al., 2017), Schoen-FRD (Sathishkumar et al., 2020), and Fisher-Koch C (Abou-Ali et al., 2019) have been produced and their mechanical properties (Soyarslan et al., 2019), physical characteristics (Al-Ketan and Abu Al-Rub, 2019), and fluid permeability (Jung and Torquato, 2005) have been studied in interpenetrating phase composites (IPCs), co-continuous composites (Poniznik et al., 2008), tissue engineering scaffolds (Blanquer et al., 2017), and other engineering applications (Al-Ketan and Abu Al-Rub, 2019). In this paper, the four most popular topologies have been considered for study.

Recent advances in additive manufacturing, and in particular, in technologies such as stereolithography (SLA), digital light processing

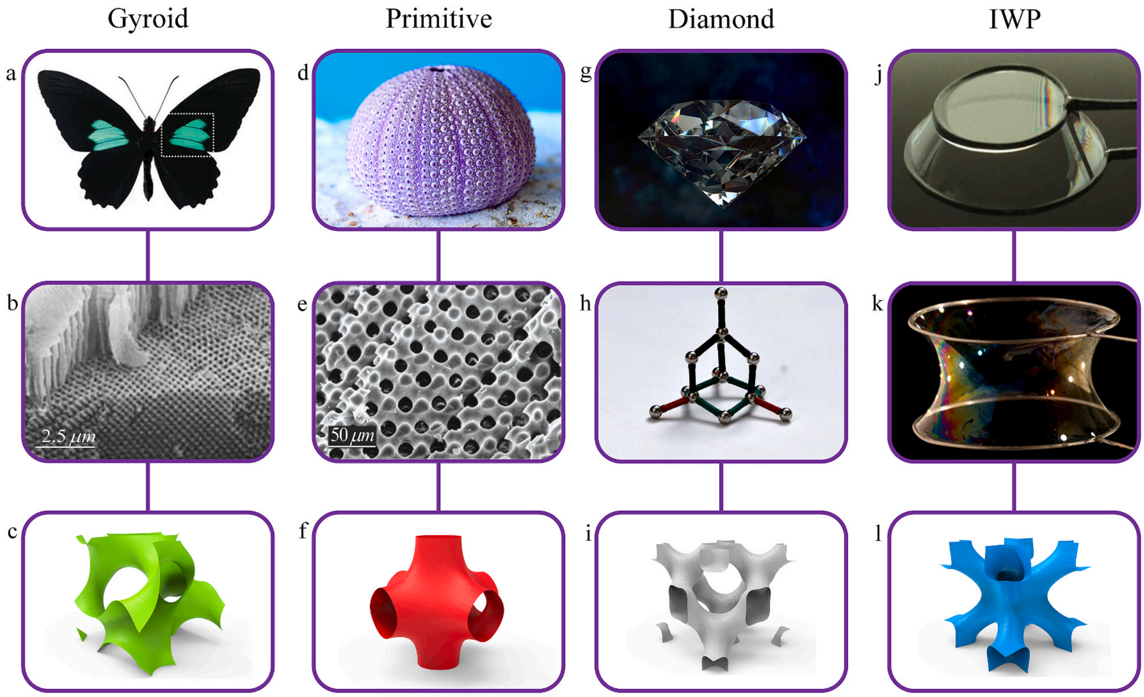

**Fig. 1.** Natural creatures inspiring the four main unit cells implemented in this study. The top row demonstrates the macro-scale visualization of the natural creature, the mid-row demonstrates the micro- or nano-scale visualization of the natural creatures, and the bottom row depicts the nature-inspired unit cells. First column: a) butterfly wings (Pouya et al., 2016), (b) micro-structure of butterfly wing (Pouya et al., 2016), and (c) gyroid TPMS-based unit cell. Second column: (d) The sea urchin, (e) micro-structure of a cross-section through a sea urchin skeletal plate (Lai et al., 2007), and (f) primitive TPMS-based unit cell. Third column: g) A diamond, h) schematic representation of molecular structure of diamond, and (i) diamond TPMS-based unit cell. Fourth column: (j) The formation of a soap film with lamella supporting the wireframes (Alimov et al., 2021), k) A soap film between two metal wires based on IWP geometry (Alimov et al., 2021), and (l) IWP TPMS-based unit cell.

(DLP), and liquid crystal display (LCD) have made it possible to use SMP-based liquid resins to fabricate SMP-based metamaterials (Yang et al., 2019) and SMP-based origami structures (Hedayati et al., 2021). In recent years, SMP- and TPMS-based metamaterials have been widely considered by researchers, separately. However, no extensive research has been dedicated to SMP metamaterials based on TPMS to systematically examine their shape-memory behavior, which has the potential of exhibiting a wide range of exotic and marvelous behaviors. Design and development of SMP metamaterials based on TPMS creates a lot of possibilities in different research and industrial fields including tissue engineering, a few examples of which will be given later in the article.

In this research, we study SMP metamaterials based on four TPMS structures that can be conveniently generated using mathematical equations and be easily fabricated by AM technologies. The responses of these meta-structures are tunable to provide SME and unusual mechanical properties. SMP properties are assigned to TPMS-based metamaterials by applying thermo-visco-hyperelastic constitutive models coupled with the time-temperature superposition principle (TTSP) to reconstruct the shape-memory behavior. Our research compares the trend of changes in the shape-memory characteristics (shape recovery, force recovery, and shape fixity) and mechanical properties (Poisson's ratio and elastic modulus) for different TPMS-based structures, level volume fractions, and filling status (filled or core-shell). Eventually, we state the applications and advantages of SMP metamaterial based on TPMS in tissue engineering field.

## 2. Materials and methods

In the first step, the surfaces of metamaterials were constructed by MathMod (virtualmeet, Canada) mathematical software. The volumetric and surface discretization of both the core-shell and filled models were performed in 3-MATIC (Materialise, Belgium). The numerical simulation of material behavior was done using finite element (FE) analysis in ABAQUS (Dassault Systèmes, France).

### 2.1. Generation and modeling of microstructures

Metamaterials based on TPMS microstructures were chosen for this research. A TPMS unit cell, which was selected to be the base of the structures in this study, is a minimal surface with translation symmetries in all three independent directions. Minimal surfaces are defined as constant and vanishing curvature $H = \frac{(k_1+k_2)}{2} = 0$. In this equation, $k_1$ and $k_2$ are two principal curvatures in two mutually orthogonal directions that have equal magnitude but opposite signs. TPMS topologies based on primitive, gyroid, diamond surfaces divide space into two congruent regions, whereas the IWP triply periodic minimal surface form a bicontinuous structure with each separate domain possessing different volumes (Soyarslan et al., 2019; Han and Che, 2018). Their surfaces could be readily produced by their specified mathematical functions. Moreover, their continuous surface geometries make them manufactural, especially through additive manufacturing methods. The main function of a TPMS geometry is $F(x, y, z) = \xi$ where $\xi$ is the level cut (Schoen, 1970; Han and Che, 2018; Mackay, 1985; Cvijovi ć and Klinowski, 1994; Michielsen and Kole, 2003). The equation of each TPMS-based structure chosen for this study is given in the following:

Primitive:

$$F(x,y,z) = a[\cos(x) + \cos(y) + \cos(z)] + b[\cos(x)\cos(y) + \cos(y)\cos(z) + \cos(z)\cos(x)] \tag{1}$$

where $(a, b) = (10, -5.0)$

Gyroid:

$$F(x,y,z) = a[\cos(x)\sin(y) + \cos(y)\sin(z) + \cos(z)\sin(x)] + b[cos(2x)\cos(2y) + cos(2y)\cos(2z) + cos(2z)\cos(2x)] \tag{2}$$

where $(a, b) = (10, -5.0)$

Diamond:

$$F(x,y,z) = a[\sin(x)\sin(y)\sin(z) - \cos(x)\cos(y)\cos(z)] + b[cos(4x) + cos(4y) + cos(4z)] \tag{3}$$

where $(a, b) = (10, -0.7)$

IWP:

$$F(x,y,z) = a[\cos(x)\cos(y) + \cos(y)\cos(z) + \cos(z)\cos(x)] + b[cos(2x) + cos(2y) + cos(2z)] \tag{4}$$

where $(a, b) = (10, -5.0)$

MathMod software was implemented to produce surfaces using the above-mentioned functions. Each $\xi$ would create different volume contained in each level cut surface ($\varphi_\xi$). The level cuts of 30, 35, 40, 45, and 50 have been considered in this study (Fig. 2). In the next step, CAD models were generated based on the surfaces through 3-Matic software. Two types of CAD models, filled and core-shell, were generated for each TPMS-based structure. In the filled model, the internal regions of the surfaces were filled, while in the core-shell ones, the surfaces were given a specific thickness. The phase volume fraction $\varphi_\beta$ of the core-shell models can be calculated from

$$\varphi_\beta = \frac{h_\rho}{\upsilon} \tag{5}$$

where $h$is the surface thickness, $\rho$ is the mid-surface area of a single unit cell, and $\upsilon$ is the volume of the unit cell. In all the TPMS-based core-shell models, a set value for phase volume fraction of $\varphi_\beta \simeq 30\%$ is considered. Only for the filled structures $\varphi_\beta = \varphi_\xi$. The values of parameters $\xi$ and $h$ can be found in Table A1 provided in Appendix A of the paper.

### 2.2. Shape-memory effect modeling using thermo-visco-hyperplastic model

Researchers have presented two main approaches to model the behavior of SMPs namely viscoelastic and phase transition (Yarali et al., 2020a). As the SMPs show complicated SME, the models which are able to predict the shape-memory behavior by taking mobility, intermolecular chain interactions, and relaxation time into account are of interest. In this study, a large deformation nonlinear thermo-visco-hyperelastic model coupled with TTSP was used. First, Westbrook et al. (2011) introduced a model with large thermal viscoelastic deformation in 2011, which was later on modified by Diani et al. (2012) and Arrieta et al. (2014). Jebellat et al. (2020) updated the model in 2020 to investigate the behavior of SMP-based smart structures and metamaterials in different topologies, and this updated approach was chosen for this study. The constitutive model consists of two hyperelastic constituents to model the behavior of large deformation regimes at high temperature as well as thermo-viscoelastic behavior related to the time. The total stress $\boldsymbol{\sigma}\,(\boldsymbol{\varepsilon}, t)$ can be defined as:

$$\boldsymbol{\sigma}\,(\boldsymbol{\varepsilon}, t) \approx \int_0^t \frac{d\boldsymbol{\sigma}_0(\boldsymbol{\varepsilon})}{d\omega}\, g(t-\omega)\, d\omega \tag{6}$$

where $\boldsymbol{\sigma}$ and $\boldsymbol{\varepsilon}$ are respectively the stress and strain second-order tensors, $\boldsymbol{\sigma}_0$ is the strain-dependent part of the stress tensor, and $g(t)$ is a dimensionless function (also known as Maxwell-Kelvin model (Brinson and Brinson, 2008)) representing the time-dependent part of stress, and it is given by

$$g(t) \approx g_\infty + \sum_{i=1}^{N} g_i \exp\left(\frac{-t}{\tau_i}\right) \tag{7}$$

where $g_\infty$ is the non-dimensional storage modulus, and $g_i$ are non-dimensional material constants obtained for Prony series and they correlate with the equilibrium ($g_\infty$) and instantaneous (viscous) parts

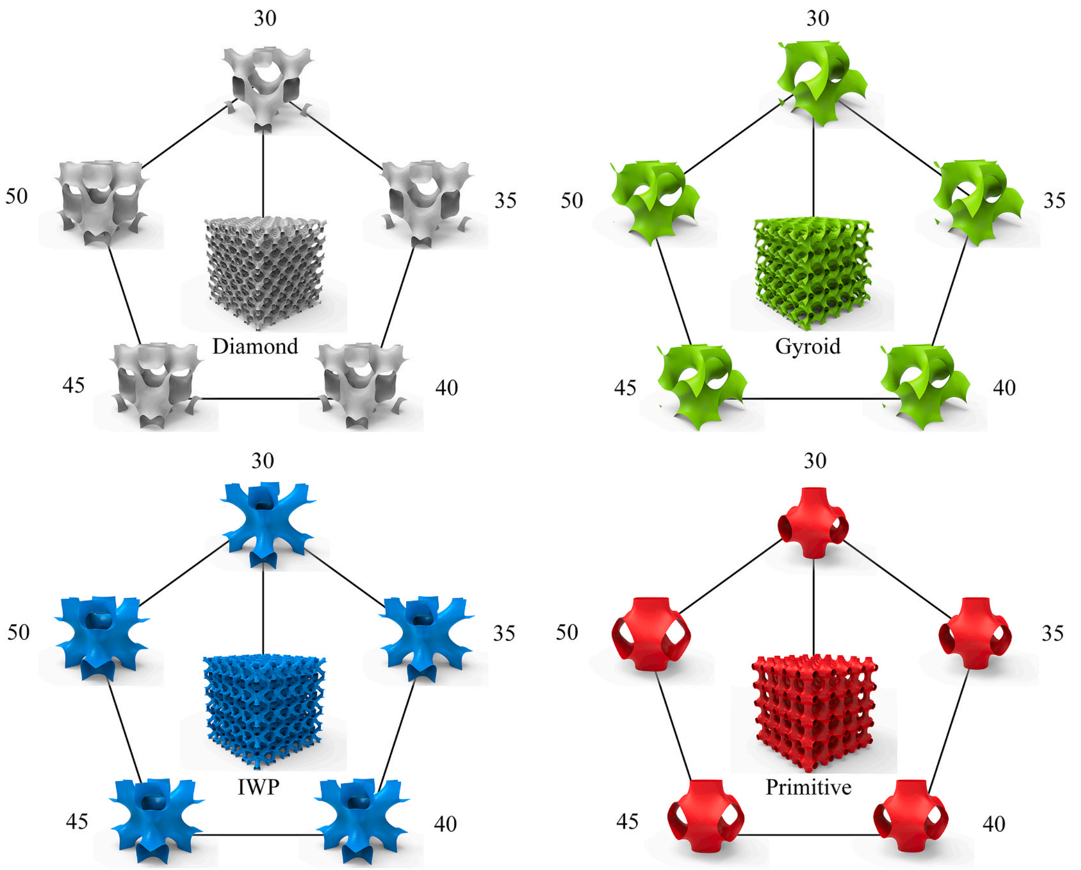

**Fig. 2.** 3D model of primitive, gyroid, diamond, and IWP microstructures based on TPMS. At the center of each diagram, the final filled lattice structure is shown, and the unit cells with different level volume fractions ($\varphi_\xi = 30\%, 35\%, 40\%, 45\%,$ and $50\%$) are demonstrated in the surrounding of each diagram.

($G_0 = g_\infty + \sum_{i=1}^{N} g_i$). The constants $g_\infty$ and $g_i$ take values between zero and 1, under constraint of $g_\infty + \sum_{i=1}^{N} g_i = 1$. Moreover, $\tau_i$ is pertaining to relaxation or retardation time in $i^{th}$branch ($i = 1, 2, 3, ..., N$ ) .To put it in another way, $\boldsymbol{\sigma}_0$ in Equation (6) represents the hyperelastic part of the deformation. The Cauchy stress $\boldsymbol{\sigma}_0$ as a function of strain energy density $\psi$ $(I_I, I_{II})$ can be written as follows (Yarali et al., 2020b; Baniasadi et al., 2020),

$$\boldsymbol{\sigma}_0(\boldsymbol{\varepsilon}) = -p\mathbf{I} + 2\left(\frac{\partial\psi}{\partial I_1} + I_I\frac{\partial\psi}{\partial I_2}\right)\mathbf{B} - 2\frac{\partial\psi}{\partial I_{II}}\mathbf{B}^2 \tag{8}$$

where $p$ is the hydrostatic pressure, and $I_i$ $(i = I, II)$ are invariants of left Cauchy-Green deformation tensor $\mathbf{B} = \mathbf{F}\mathbf{F}^{\mathbf{T}}$ (where $\mathbf{F}$ is the deformation gradient tensor). For the strain energy function, the neo-Hookean formula is considered:

$$\psi = C_{10}(I_I - 3) \tag{9}$$

where $C_{10}$ is the material parameter. The invariants of the left-hand Cauchy-Green tensor are

$$\begin{aligned} I_I &= \mathrm{tr}\,(\mathbf{B}) \\ I_{II} &= \frac{1}{2}\left[(tr(\mathbf{B}))^2 - tr(\mathbf{B}^2)\right] \\ I_{III} &= \det\,(\mathbf{B}) \end{aligned} \tag{10}$$

In order to consider the temperature effect (i.e., softening/stiffening effect) in the SME path, the time-temperature superposition principal was used. According to this theory, time scale and temperature are coupled. In other words, in Equation (7), $t$ can be replaced by the parameter $t'$ defined as:

$$t' = \int_{\omega=0}^{\omega=t} \frac{d\omega}{a\,(T)} \tag{11}$$

where $a(T)$is known as the shift factor function, as it shifts the shear modulus at different temperatures. To do that, the dynamic-mechanical-thermal analysis (DMTA) was performed and shape factors were extracted from the obtained curves. The variation of the storage modulus $E'$ and the loss modulus $\tan\,(\delta)$ with temperature is shown in Fig. C1 in Appendix C. An important empirical relationship for predicting the TTSP is Williams-Landel-Ferry (WLF) formula (Brinson and Brinson, 2008). WLF formula is usually used at temperatures above $T_g$ (Brinson and Brinson, 2008). In this study, the WLF equation,

$$\log\,(a(T)) = \frac{-C_1(T(t) - T_r)}{C_2 + (T(t) - T_r)} \tag{12}$$

was used for TTSP, where $C_1$ and $C_2$ are material constants, $T(t)$ is the time-dependent temperature, and $T_r$ is the reference temperature. All the material parameters can be found in Table B1 provided in Appendix B.

An acrylate network composition proposed and implemented in (Arrieta et al., 2014; Safranski and Gall, 2008) was employed for the bulk material. The polymer is prepared by the copolymerization of benzyl methacrylate (BMA) with poly (ethylene glycol) dimethacrylate (PEGDMA) of molar weight $550g/mol$. Photopolymerized materials synthesized from a tert-butyl acrylate monomer with a moderate amount of a diethyleneglycol diacrylate crosslinker show good shape recovery. Due to their biocompatibility and their capacity for photopolymerization, these materials have significant potential for biomedical applications (Gall et al., 2005).

Three parameters of shape recovery, force recovery, and shape fixity are usually implemented by researchers to examine the shape-memory effect in SMP. In this study, SME cycle of metamaterials in tension mode is studied. The schematic of the shape recovery process, force recovery process, strain-time diagram, and temperature-time diagram are shown in Fig. 3. The common steps of both the shape recovery and force recovery processes are described in the following sentences. In the zero step, the specimen is preheated to a high temperature $T_H$ above the glass transition temperature $T_g$, which is required for experimental works, whereas in the numerical simulations the sample is placed at a high temperature from the beginning. In the first step, the specimen is kept at $T_H$ to arrive at an isothermal condition, and a pre-specified tensile load is applied to the specimen. In the second step, the specimen is cooled down to a low temperature $T_L$, which is lower than $T_g$, while it is constrained. In the third step, the specimen is unloaded, which would cause a small elastic spring back strain, known as shape fixity (its percentage can be calculated relative to the initial displacement). Finally, the fourth step is heating to $T_H$ or the recovery process.

The difference in the shape recovery and force recovery processes are explained in the following. As for the shape recovery test, after unloading, the specimen is reheated to $T_H$, because of which the specimen is prone to be transformed into its original shape. The ratio of shape transformation extent to the original length is called shape recovery (step 4i):

$$R = \frac{X_d - X_{nr}}{X_d} \times 100\% \tag{13}$$

where $R$ is shape recovery in percentage, $X_d$ is the extent of maximum displacement applied to the structure, and $X_{nr}$ is the non-recovered length at $T_H$ after shape recovery. Another critical parameter in SMPs is Shape fixity defined as the capability of SMP in keeping its temporary shape during the programming process. The percentage of shape fixity $R_F$ in a thermomechanical cycle can be calculated by

$$R_F = \frac{L_T}{L_D} \times 100\% \tag{14}$$

where $L_T$ is the length of the structure (in direction of loading) after the unloading step, and $L_D$ is the length at the end of the cooling process. On the other hand, during the force recovery process, the specimen is held fixed and is heated up to $T_H$. By changing the temperature and phase transition, the specimen tends to regain its original shape, but since the specimen is constrained, it starts to develop a force. The ratio of the force generated after heating in the final step $F_{FR}$, to the force required to program the initial deformation in the specimen $F_{Pre}$, is defined as the force recovery ratio $F_{FR}$, (step 4ii):

$$R_{FR} = \frac{F_{FR}}{F_{Pre}} \times 100\% \tag{15}$$

For a better understanding of the shape-memory cycle, a diagram in terms of three affecting parameters related to the shape-memory behavior (stress, strain, and temperature) is depicted in Fig. 3e.

## 3. Results and discussion

In this section, the results from the shape and force recoveries, shape fixity, and some mechanical properties (elastic modulus and Poisson's ratio) are examined for different level volume fractions, topologies, and filling status (filled or core-shell).

In Fig. 4, the simulation steps and results for one of the specimens (IWP geometry with $\varphi_\xi = 50\ \%$) are presented. The simulation steps (4

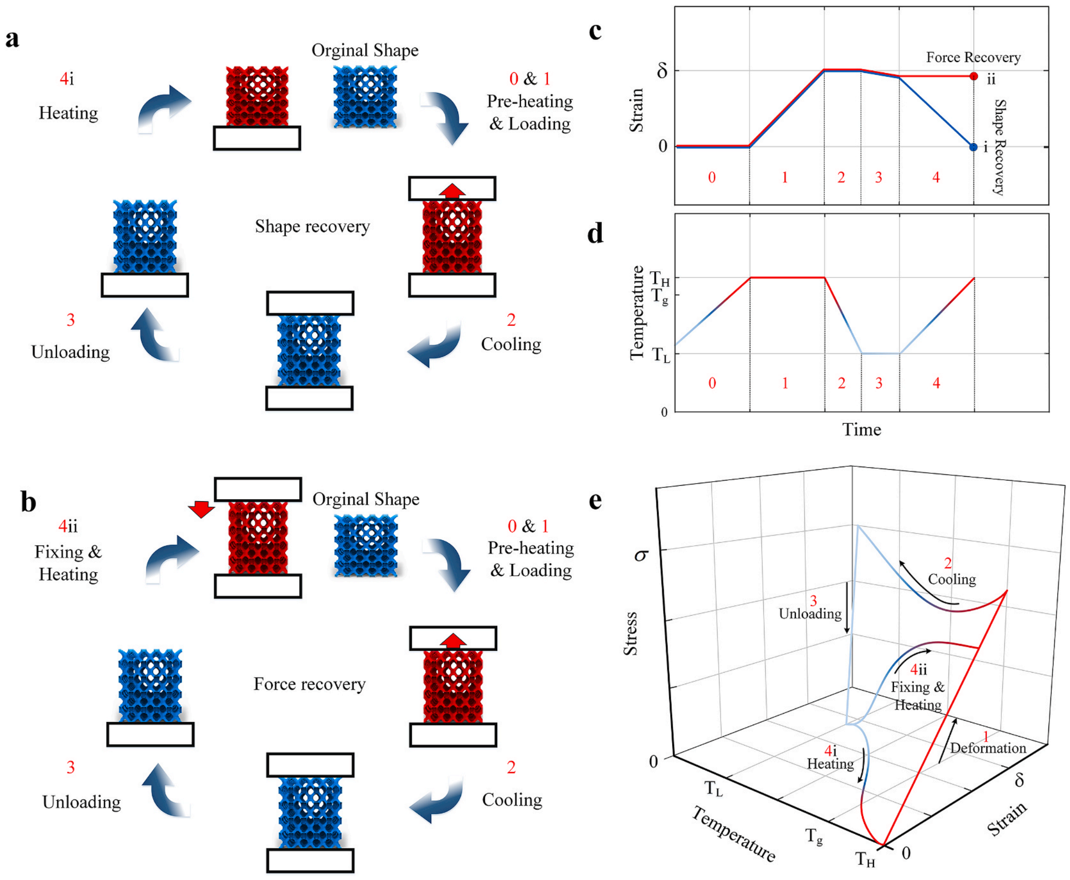

**Fig. 3.** Shape-memory behavior of SMP: a) schematic of shape recovery cycle in compression mode, b) schematic of force recovery cycle in compression mode, c) the strain-time diagram, d) the temperature-time diagram, and e) 3D diagram of SMP shape-memory cycle in terms of stress, strain, and temperature.

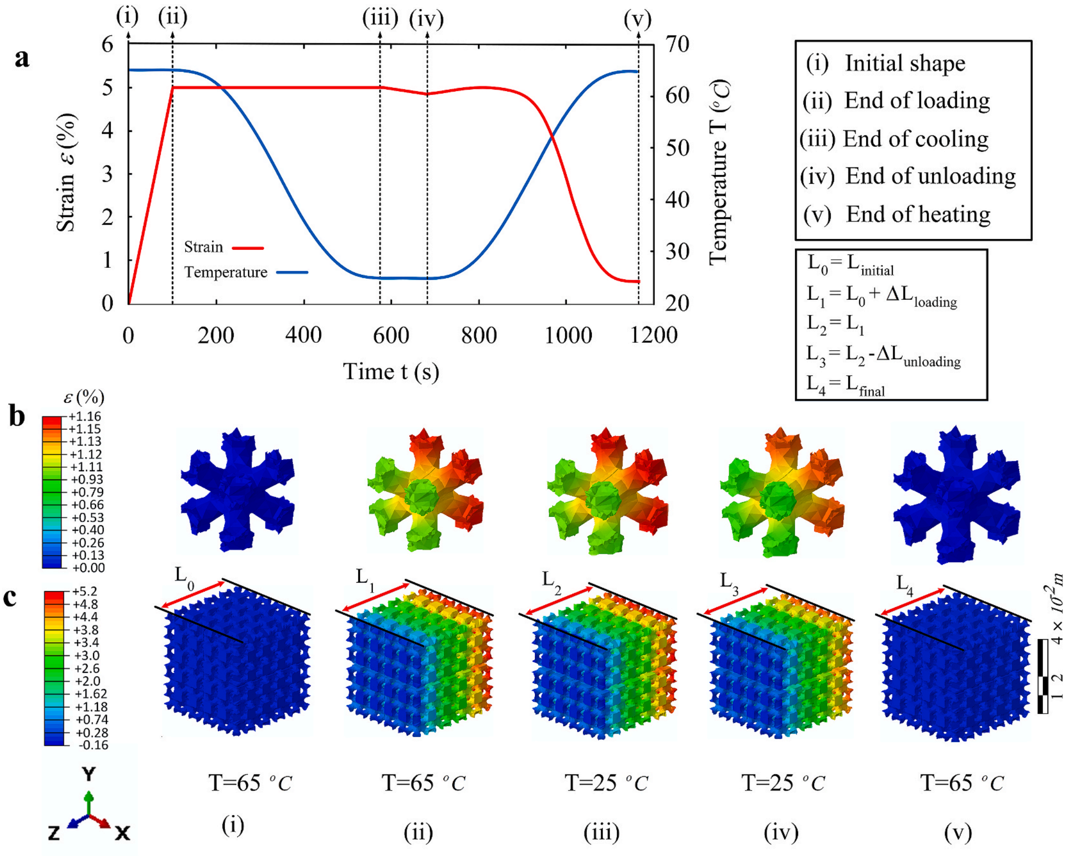

**Fig. 4.** Thermomechanical cycle, a) applied strain versus time plot in the shape-memory effect path, b) overall strain variations in the same path of a unit cell located in the back side of the IWP lattice structure, c) overall strain variations in the same path for the whole lattice, which recovers its initial shape after a cycle.

steps in total), strain contours in each unit cell at each state at the end of each step, as well as the strain contours in the lattice structure at the end of each step are illustrated in this figure. In the first state (i), the lattice has its initial shape with the initial length of $L_0$. During the loading (Step 1), the structure is under 5% tensile strain in the –Z-direction at the XY plane at 65 °C until $t = 100\ s$, and at the end of this step, in state (ii), the length is $L_0 + \Delta L_{loading}$. During cooling (Step 2), until $t = 580\ s$, the temperature is reduced to 25 °C at a rate of 5 °C/min while the structure is constrained, meaning that the length at state (iii) is the same as the previous state. During unloading (Step 3), up to $t = 680\ s$, a tiny amount of the strain is recovered elastically and the new length at state (iv) is equal to $L_0 + \Delta L_{loading} - \Delta L_{unloading}$. Finally, during heating (Step 4), the lattice is heated up at a rate of 5 °C/min, which triggers the shape recovery due to the increase in temperature to $T > T_g$, and at $t = 1160\ s$ in

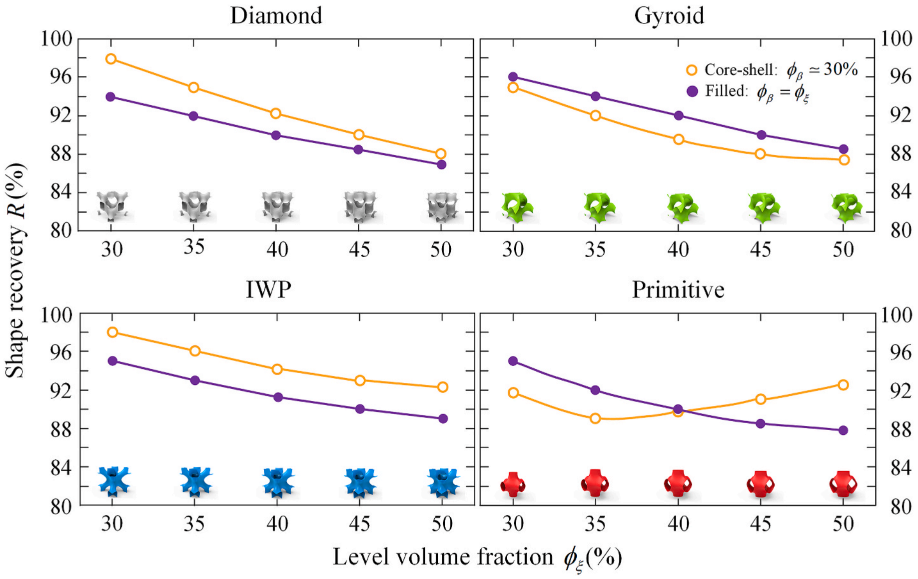

**Fig. 5.** Shape recovery percentage for various level of $\varphi_\xi$ for filled and core-shell models.

state (v) the final length is $L_{final}$, and the lattice recovers its initial shape. It is shown in the strain-time diagram (Fig. 4a) that a shape recovery up to 89% occurs. The state of the lattice structure at the end of different steps are demonstrated in Fig. 4b,c.

### 3.1. Shape recovery

The shape recovery percentage for each geometry and for both filled and core-shell unit cells in the last step (Step 5i in Fig. 3), was calculated at different volume fractions (30% $< \varphi_\xi <$ 50 %, see Fig. 5). Shape recovery ratio had a reverse correlation with $\varphi_\xi$ in all topologies except for the core-shell primitive model at $\varphi_\xi >$ 35%, where an increase in $\varphi_\xi$ enhanced the shape recovery. It is observed that an SMP material provides a higher shape recovery when loaded in flexural mode as compared to when it is under uniaxial loading (Roudbarian et al., 2019b). For the case of force recovery, the opposite holds true (Roudbarian et al., 2019b); in other words, a higher force recovery was observed in uniaxial deformation mode as compared to flexural mode. In the filled TPMS-based lattices, as the level volume fractions increased, the flexural stress contribution in the total stress distribution in the walls decreased, which lowered the shape recovery. This is due to the higher percentage of the material bulk, which is aligned with the direction of the applied load. On the other hand, in the core-shell TPMS-based lattices, since $\varphi_\beta \simeq$ 30% is the same for all the level volume fractions ($\varphi_\xi$), the thickness of TPMS-based structure is decreased by increasing $\varphi_\xi$. Under an equal applied strain, a decrease in the thickness of TPMS-based structure will lead to higher local strains and stresses in the core-shells, which results in lower shape recovery ratios for higher $\varphi_\xi$.

The maximum shape recovery occured at the lowest $\varphi_\xi$ (i.e., 30%) in all geometries. The maximum shape recovery belonged to the core-shell diamond model (with 98% shape recovery). In the diamond and IWP geometries, the core-shell models had higher shape recoveries compared to the filled models. However, in the gyroid geometry, the filled models had higher shape recoveries in comparison to core-shell ones. On the other hand, for the primitive geometry, up to $\varphi_\xi$ = 40%, the filled structures had higher shape recoveries as compared to core-shell ones, whereas after $\varphi_\xi$ = 40%, an opposite trend was observed.

### 3.2. Shape fixity

Shape fixity is the ability of SMP in keeping its length after removing the applied stress (Fig. 3, Step 4). In most cases, SMPs experience a reduction in length when the programming stress is removed. Complete (i.e., 100%) shape fixity, the ideal situation for an SMP, occurs only when there is no length reduction in the shape-memory effect cycle. The shape fixity for different geometries and $\varphi_\xi$, and for both the filled and core-shell configurations, are depicted in Fig. 6. The difference of shape fixities (due to spring back effect) between the filled and core-shell specimens was very small, except for the IWP and primitive at high level volume fractions ($\varphi_\xi$ = 50%). Nonetheless, the maximum difference in the shape fixity of the core-shell and filled specimens was very small (i.e., <4%). Unlike the shape recovery curves (Fig. 5), shape fixity increased as a result of increase in $\varphi_\xi$, and the stability of the temporary shape enhanced. Based on the aforementioned reasons explained for the increase in the shape recovery, an opposite behavior occured for the shape fixity. Strictly speaking, superiority in the shape recovery contributes to diminished shape fixity. Among all the specimen types, the highest shape fixity extents belong to the filled IWP specimen with a maximum shape fixity of 98%, and core-shell primitive specimen with a maximum shape fixity of 97% (Fig. 6).

### 3.3. Force recovery

In many applications, force recovery magnitude is of more importance than the shape recovery extent. A good example of such applications is actuation by force in bounded systems. An SMP with high shape recovery but low force recovery is not useful in such instances.

The behavior of the force recovery ratio was similar to that of shape fixity, meaning that it had a positive correlation with $\varphi_\xi$ in all geometry types, and in both the filled and core-shell configurations (Fig. 7). The reason why force recovery increases by increase in the level volume fraction can be explained as follows. By increasing the level volume fraction, a higher percentage of the bulk material is aligned with the external uniaxial load applied. As it has been observed before, an SMP material gives a higher force recovery ratio when it is loaded in uniaxial mode as compared to when it is loaded in flexure. This leads to higher

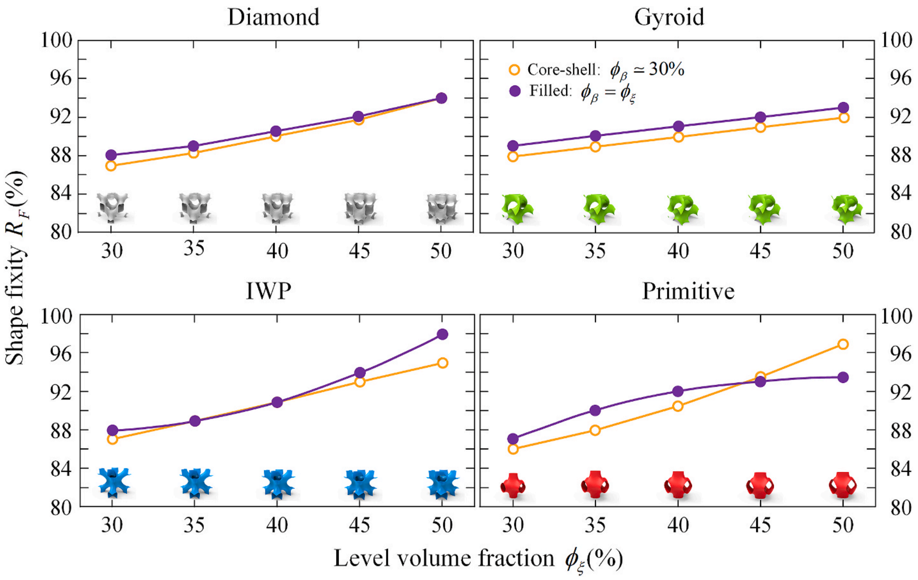

**Fig. 6.** Shape fixity percentage for various level of $\varphi_\xi$ for filled and core-shell models.

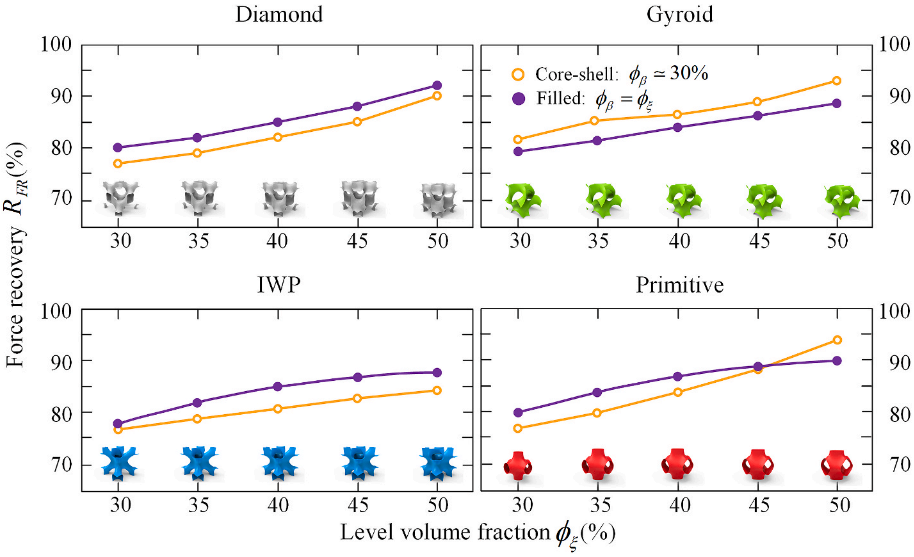

**Fig. 7.** Force recovery percentage for various level of $\varphi_\xi$ for filled and core-shell models.

force recoveries in the filled TPMS-based lattices when the level volume fraction of the material increases. On the other hand, in the core-shell TPMS-based lattices, higher local stresses (due to decrease in the thickness) lead to better force recoveries when the level volume fraction of the material increases.

The highest force recovery ratio belongs to the core-shell primitive and gyroid geometries with a force recovery of ~94%, followed by the filled diamond geometry with about 93% force recovery.

### 3.4. Mechanical properties

The mechanical properties, including the Poisson's ratio and the elastic modulus, were obtained at the end of loading step where $T > T_g$ and applied strain was 5%. The Poisson's ratio in the gyroid and IWP structures (in both the filled and core-shell configurations) decreased continuously by increasing $\varphi_\xi$ (Fig. 8). The same results applied to the filled diamond case. However, in the core-shell diamond structure, by increasing $\varphi_\xi$, the Poisson's ratio first decreased and then rised. On the contrary, the Poisson's ratio had a negative correlation with $\varphi_\xi$ in the case of primitive geometry (in both the core-shell and filled configurations). The Poisson's ratio value in the filled and core-shell configurations of gyroid and IWP geometries remained close. Additionally, change in $\varphi_\xi$ value did not make a significant difference in the Poisson's ratio of these geometries. However, in the diamond and primitive core-shell geometries, a completely nonlinear behavior for the Poisson's ratio was observed, whereas their filled structures had linear curves. The highest value of the Poisson's ratio belonged to the filled and core-shell IWP geometry, which was around 0.5, and the lowest Poisson's ratio value was associated with the filled primitive geometry with $\varphi_\xi = 30\%$ and core-shell diamond geometry with $\varphi_\xi = 45\%$, both being around 0.1.

Increasing level volume fraction changes the surface topology as the surface functions of TPMS-based structures are highly dependent on $\xi$. The effect of this change in topology is different for different unit cell

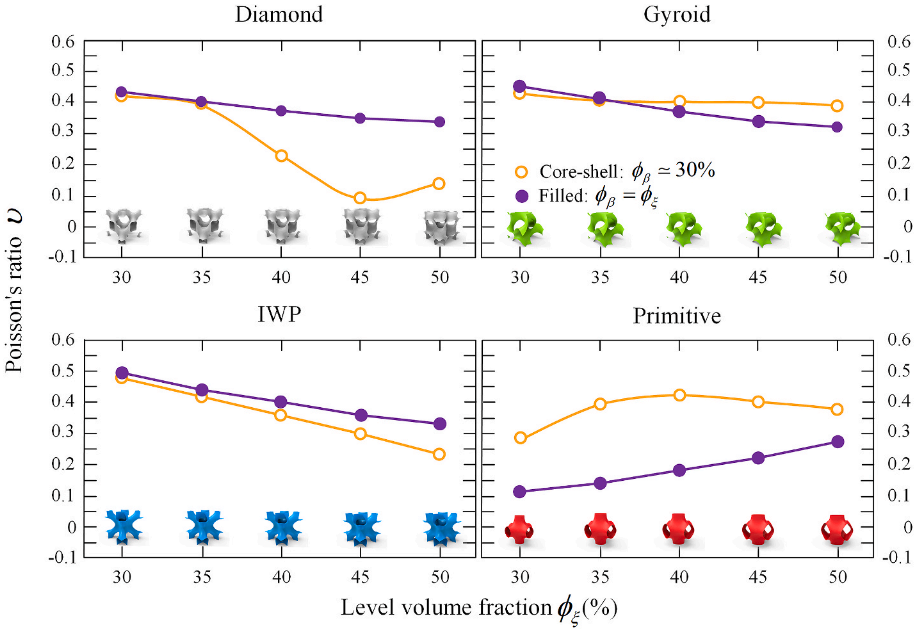

**Fig. 8.** Poisson's ratio for various level of $\varphi_\xi$ for filled and core-shell models.

types. In gyroid and IWP unit cells, increasing the level volume fraction did not significantly change the topological configurations. In other words, in the gyroid and IWP topologies, the orientation of the surfaces varied only slightly as a result of change in the level volume fraction. That is why these two structures did not demonstrate a significant change in the Poisson's ratio with respect to the level volume fraction variations. However, in the diamond structure, the fraction of oblique surfaces decreased as a result of increase in level volume fraction. In other words, the main mode of deformation in the walls changed from flexure to axial. This led to an exponential decrease in the Poisson's ratio in the diamond core-shell structure with respect to the volume fraction increase. In the primitive structure, however, the opposite holds true, meaning that increasing the volume fraction led to a structure with a higher fraction of oblique walls. This enhances the contribution of flexure in the total deformation of the structure, which means it magnifies the lateral displacement of the whole structure. That is why in the primitive structure, by increasing the volume fraction, unlike the other structures, the mentioned mechanism (i.e., change in the deformation mode from axial to bending) increases the Poisson's ratio.

The normalized elastic modulus (elastic modulus of the lattice divided by the elastic modulus of the constituent material, $E_0 = 5.74\,MPa$) variations of different topologies at high-temperature are shown in Fig. 9, where the stiffness has a continuous direct correlation with the material level volume fraction, regardless of being core-shell or filled. At the level volume fraction of $\varphi_\xi = 50\%$, the lowest and highest normalized elastic moduli for the filled-configurations belong to the diamond $(E/E_0 = 0.61)$ and primitive $(E/E_0 = 0.46)$ topologies, respectively. On the other hand, in the core-shell models $(\varphi_\xi = 50\%)$, the minimum and maximum normalized elastic moduli are associated with primitive $(E/E_0 = 0.31)$ and IWP $(E/E_0 = 0.41)$unit cells, respectively.

The reason behind different trends in change of elastic modulus can be described by the same mechanism explained for the Poisson's ratio. Surface topologies are highly dependent on $\xi$. Increasing the level volume fraction has different effects on the topology variation in different unit cell types. In two of the unit cells, i.e., gyroid and IWP, increasing the level volume fraction does not significantly affect the topological configurations. In other words, in the gyroid and IWP topologies, the angles of the surfaces vary only slightly upon a change in the level volume fraction. However, in the diamond structure, the fraction of oblique surfaces is reduced as a result of increase in level volume fraction, meaning that the main mode of deformation in the walls transforms from flexure to axial. This leads to a sharp rise in the elastic modulus of the diamond structure in terms of level volume fraction increase. In the primitive structure, however, the opposite holds true, i.e., increasing the level volume fraction gives a structure with a higher fraction of oblique walls. This enhances the contribution of flexure in total deformation of the structure, which means it diminishes the stiffness of the whole structure. Another mechanism also contributes to the elastic modulus of most of topologies. When the level volume fraction grows, the pore sizes obviously increase in the IWP and primitive structures. Increase in pore sizes amplifies the flexural stiffness of the elements and thus the whole structure. That is why in the primitive structure, by increasing the level volume fraction, even though the stiffness is enhanced due to a higher flexural stiffness, the first aspect (i.e., change in the deformation mode from axial to bending) slows down the increase.

### 3.5. Potential application areas

Extensive commercial applications of the SMPs have attracted the attention of various industries, but according to Dietsch and Tong (2007), 50–70% of patents filed related to SMP are in the field of medical science. Researchers have suggested many biomedical applications for these materials. For instance, SMP sutures could be designed in such a way that they contract after being applied on an injured tissue and then rising the temperature locally, which leads to quick closure of wounds (Lendlein and Langer, 2002). The temperature increase could be applied by the surgeon when implanting the SMP in the body and by means of a device that would only influence the SMP and not the surrounding tissues/bone. For instance, such location-specific heating could be accomplished by mixing elements such as nano-particles in the SMP, which are sensitive to external stimuli such as an electromagnetic field. In addition, attention to smart materials in recent years has led to the tendency of using these materials in the manufacturing of smart stents. Increase in the temperature of smart stents would cause stimulation in the stent and therefore eliminates the need for traditional complex stimuli such as balloons (Yakacki et al., 2007; Ward Small et al., 2010). Another main application of SMPs, that has received a lot of attention and efforts recently, is tissue engineering and repairing bone defects with critical size (Xie et al., 2018).

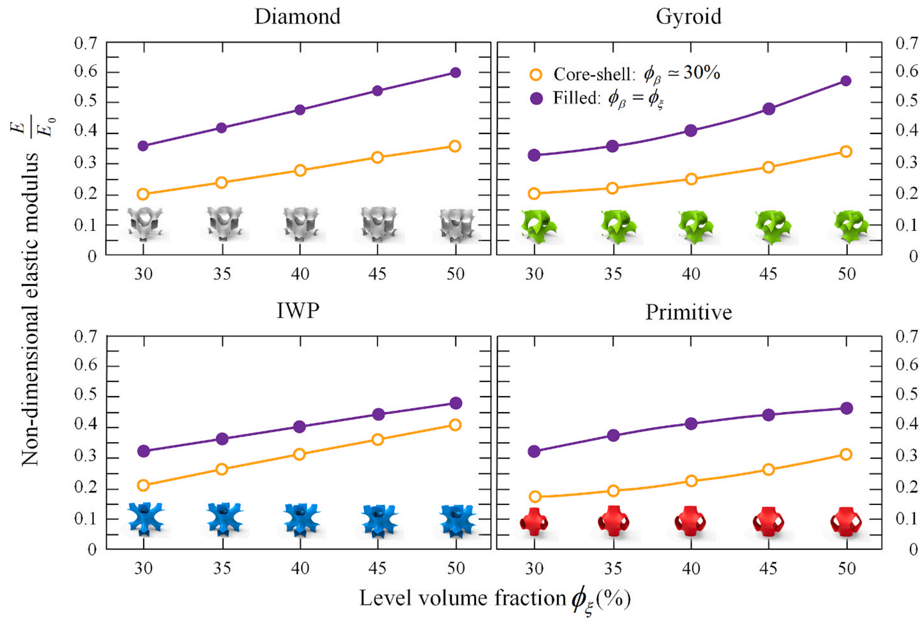

**Fig. 9.** Non-dimensional elastic modulus for various levels of $\varphi_\xi$ for filled and core-shell models.

Critical bone defects, which may be caused by injury, tumor excision, and congenital defects, do not improve without intervention (Spicer et al., 2012). For orthopedic surgeons, reconstruction of a large bone defect has been a major challenge (Gruskin et al., 2012). Bone tissue engineering is one of the most critical methods for treating bone defects, especially relatively large bone defects. In particular, the porosity of biological materials plays an essential role in osseointegration and osteoconduction and supports the migration of cells, capillary ingrowth, and the transport of nutrients to the cells (Karageorgiou and Kaplan, 2005; Ahmadi et al., 2018). The advantage of the metamaterials introduced in this study is that they can be designed for specific bone defects and be tailored with different porosities depending on each patient's specific need. Here, metamaterials can play a key role in improving the functionality of an implanted scaffold designed for providing bone regeneration in bone defects. Fig. 10 shows a schematic of a particular bone defect: cavities with critical size in the patient's bone. The patient's bone defect can be identified by 3D image scanning. According to the patient's condition and requirement, a special type of TPMS-based lattice structure made from SMP can be designed and printed via additive manufacturing. Fig. 10 also indicates a cross-sectional view of the patient's humerus. After placing the damaged sections of the two bone segments on top of each other, a thin layer of micro-sized lattice plate made of SMP metamaterials TPMS-based microstructures is rolled and attached around the fractured area. After the SMP lattice plate is placed inside the body, its temperature is increased, which as pre-programmed, make it shorten axially (self-fitting). This transformation allows the two damaged bone segments fit together well and remain in such way preventing loosening and speeding up bone fracture repair.

Another type of bone defect that may occur as a result of congenital disease is the presence of cavities in the patient's pelvis (Fig. 10). In this type of bone defect, for bone remodeling, the SMP must behave in the opposite way to the one described above. In other words, the SMP lattice structure should be programmed in such a way that after being placed in the cavity, its size increases due to temperature rise. This leads to a good self-fitting behavior for the scaffold implanted in the bone defect, which would in turn let the cavity be filled completely. The topology of TPMS-based structure, as it is porous and as it has a lot of curvatures, is highly suitable for bone and muscle cell growth. Besides, the Poisson's ratio of the structure must be chosen to be close to the Poisson's ratio of the bone surrounding it. Otherwise, differences in the lateral motion of the bone and the scaffold can lead to their deboning upon application of an external load.

## 4. Summary and conclusions

In this study, four types of widely used TPMS-based geometries (diamond, gyroid, IWP, and primitive) were employed to construct SMP lattice structures in different volume fractions. A thermo-visco-hyperelastic constitutive model was utilized to model the mechanical behavior of SMP. The TPMS-based geometries were produced in two configurations, filled and core-shell. The trends of the shape recovery, shape fixity, Poisson's ratio, and force recovery were examined for different volume fractions.

Shape recovery generally had a negative correlation with growth in the volume fraction (except for the case of core-shell primitive model with $\varphi_\xi > 35\%$), while shape fixity and force recovery for all the geometries (in both filled and core-shell configurations) had a positive correlation with $\varphi_\xi$. Being filled or core-shell did not have a significant effect on the shape fixity of the TPMS-based lattices with their maximum difference being 4%. However, being filled or core-shell had a significant impact on the Poisson's ratio in the diamond and primitive geometries. The variations of Poisson's ratio with respect to the volume fraction in the filled diamond and filled primitive structures were linear, whereas they were nonlinear in the corresponding core-shell geometries.

The results of this study demonstrated the high influence of geometric design and volume fraction on the shape-memory behavior in SMPs and their Poisson's ratio. In some applications, the capability of the SMP in recovering its initial shape, i.e., high shape recovery, is of great importance for programming. On the other hand, in some applications such as actuators and sensors, the force recovery capability and/or displacement extents in other axes are of more importance. According to the applications and requirements in different fields, a specific geometry and volume fraction can be chosen. The wide range of SMP TPMS-based topologies, volume fractions, and configurations (core-shell or filled) introduced in this study for metamaterials can be advantageous for all the above-mentioned requirements. The other benefit of the chosen geometries is their high production capability, as these geometries are constructed by surfaces based on continuous mathematical equations, which can be easily tailored according to the need.

## Credit author statement

Nima Roudbarian: Conceptualization, Methodology, Structural Design, Formal Analysis, Investigation, Visualization, Writing- Original Draft and Editing, Project Administration. Ehsan Jebellat: Methodology,

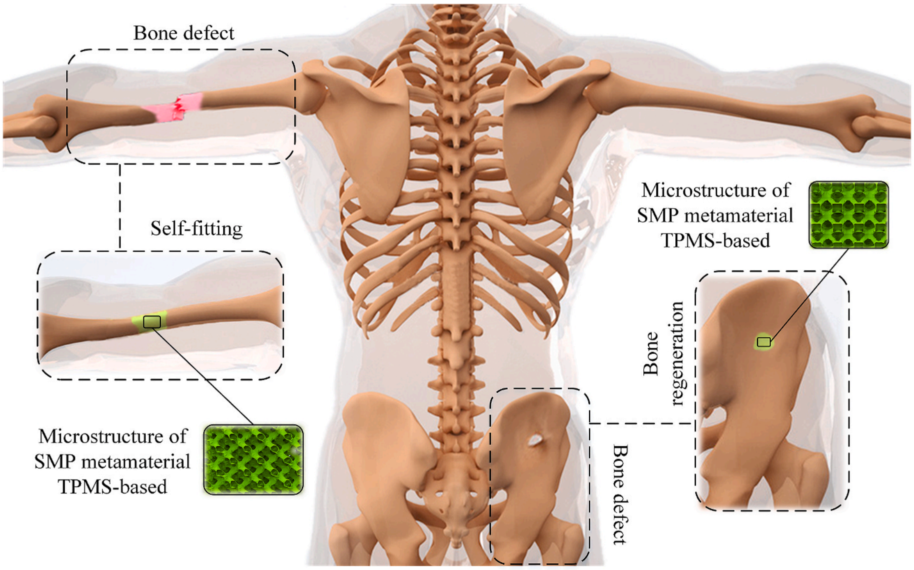

**Fig. 10.** Schematic of application of self-fitting SMP metamaterial TPMS-based lattice structure and bone regeneration TPMS-based SMP scaffolds in human skeleton.

Constitutive Modeling, Finite Element Analysis, Formal Analysis, Investigation, Writing- Review and Editing. Seyedfarzad Famouri: Methodology, Structural Design, Writing- Original Draft. Mahdi Baniasadi: Methodology, Visualization, Writing- Review and Editing. Reza Hedayati: Supervision, Investigation, Writing- Review and Editing. Mostafa Baghani: Supervision, Methodology, Investigation, Writing- Review and Editing.

## Declaration of competing interest

The authors declare that they have no known competing financial interests or personal relationships that could have appeared to influence the work reported in this paper.

## Appendix A. Geometry generation

The level cut $\xi$ and the wall thickness $h$ values of the developed unit cells based on triply periodic surfaces are listed in Table A1. The relationship between $\varphi_\xi$ and $\xi$ is defined as $\xi(\varphi_\xi) = \gamma_1\varphi_\xi^2 + \gamma_2\varphi_\xi + \gamma_3$, where $\gamma_1 = -1.466$, $\gamma_2 = -25.36$, and $\gamma_3 = 12.66$ are fitting parameters for diamond; $\gamma_1 = -2.54$, $\gamma_2 = -29.49$, and $\gamma_3 = 15.17$ are fitting parameters for gyroid; $\gamma_1 = -19.54$, $\gamma_2 = -19.19$, and $\gamma_3 = 15.6$ are fitting parameters for IWP; and $\gamma_1 = -21.25$, $\gamma_2 = -13.75$, and $\gamma_3 = 15.32$ are fitting parameters for primitive topologies.

**Table A1**
The parameters used for generating TPMS-based structures (Soyarslan et al., 2019).

| Diamond | | | | Gyroid | | | |
|---|---|---|---|---|---|---|---|
| $\varphi_\xi$[%] | $\varphi_\beta$[%] | $\xi$ | $h$ | $\varphi_\xi$[%] | $\varphi_\beta$[%] | $\xi$ | $h$ |
| 30 | 30 | 4.920 | 0.838 | 30 | 30 | 6.090 | 1.043 |
| 35 | 30 | 3.572 | 0.805 | 35 | 30 | 4.519 | 1.007 |
| 40 | 30 | 2.240 | 0.784 | 40 | 30 | 2.942 | 0.985 |
| 45 | 30 | 0.930 | 0.771 | 45 | 30 | 1.371 | 0.972 |
| 50 | 30 | −0.338 | 0.767 | 50 | 30 | −0.188 | 0.967 |
| IWP | | | | Primitive | | | |
| $\varphi_\xi$[%] | $\varphi_\beta$[%] | $\xi$ | $h$ | $\varphi_\xi$[%] | $\varphi_\beta$[%] | $\xi$ | $h$ |
| 30 | 30 | 8.082 | 0.918 | 30 | 30 | 9.275 | 1.370 |
| 35 | 30 | 6.467 | 0.883 | 35 | 30 | 7.886 | 1.132 |
| 40 | 30 | 4.770 | 0.861 | 40 | 30 | 6.396 | 1.283 |
| 45 | 30 | 2.993 | 0.848 | 45 | 30 | 4.816 | 1.262 |
| 50 | 30 | 1.157 | 0.843 | 50 | 30 | 3.153 | 1.253 |

## Appendix B. Thermo-visco-hyperelastic properties

The material parameters including viscoelastic, hyperelastic, thermal, TTSP, and general parameters are provided in Table B1.

**Table B1**
Thermo-visco-hyperelastic material parameters for the proposed SMP, adopted from (Jebellat et al., 2020).

| | | | | | | | | | | |
|---|---|---|---|---|---|---|---|---|---|---|
| Viscoelastic material parameters of SMP | | | | | | | | | | |
| $g_1 - g_{10}$ $(-)$ | 1.8706E-01 | 1.5840E-01 | 1.3761E-01 | 1.2378E-01 | 1.1283E-01 | 9.8684E-02 | 7.5819E-02 | 4.7521E-02 | 2.4477E-02 | 1.1651E-02 |
| $g_{11} - g_{20}$ $(-)$ | 5.8277E-03 | 3.1949E-03 | 1.8477E-03 | 1.0527E-03 | 5.6387E-04 | 2.8586E-04 | 1.4378E-04 | 7.4217E-05 | 3.9113E-05 | 2.0746E-05 |
| $\tau_1 - \tau_{10}$ $(s)$ | 1.26E-06 | 2.94E-06 | 6.87E-06 | 1.60E-05 | 3.75E-05 | 8.75E-05 | 2.04E-04 | 4.78E-04 | 1.12E-03 | 2.61E-03 |
| $\tau_{11} - \tau_{20}$ $(s)$ | 6.08E-03 | 1.42E-02 | 3.32E-02 | 7.75E-02 | 1.81E-01 | 4.23E-01 | 9.88E-01 | 2.31 E+00 | 5.39 E+00 | 1.26 E+01 |
| Hyperelastic material parameters of SMP | | | | | | | | | | |
| $C_{10}$ $(Pa)$ - Instantaneous | | | | | | | | | | 109,730,000 |
| $D_1$ $(Pa^{-1})$ - Instantaneous | | | | | | | | | | 1.745e-009 |
| General material parameter of SMP | | | | | | | | | | |
| $\rho$ $(kg/m^3)$ | | | | | | | | | | 1200 |
| WLF equation parameters of SMP | | | | | | | | | | |
| $T_{ref}$ $(^\circ C)$ | | | | | | | | | 80 | |
| $C_1$ $(-)$ | | | | | | | | | 6.9 | |
| $C_2(^\circ C)$ | | | | | | | | | 87.9 | |
| Thermal material parameters of SMP at $\dot{T} = 5\ ^\circ\mathrm{C/min}$ | | | | | | | | | | |
| $\alpha$ $(1/^oC)$ | 1.1741E-04 | 1.2162E-04 | 1.2589E-04 | 1.3229E-04 | 1.4066E-04 | 1.4997E-04 | | | | |
| $T(^\circ C)$ | 20 | 25 | 30 | 35 | 40 | 45 | | | | |
| $\alpha$ $(1/^oC)$ | 1.5868E-04 | 1.6658E-04 | 1.7326E-04 | 1.7811E-04 | 1.8170E-04 | 1.8425E-04 | | | | |
| $T(^\circ C)$ | 50 | 55 | 60 | 65 | 70 | 75 | | | | |

## Appendix C.  ynamic-mechanical-thermal analysis results

The variation of the storage modulus $E^{'}$ and the loss modulus $\tan(\delta)$ with temperature based on DMTA results are shown in Fig. C1.

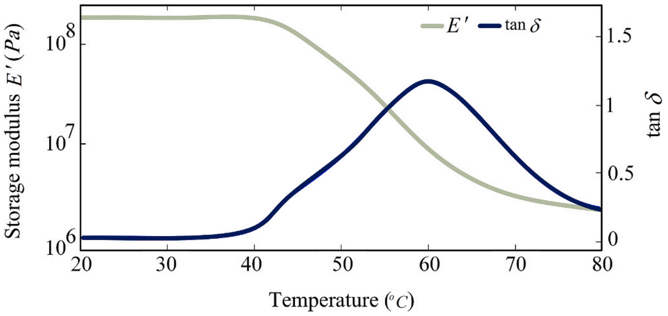

**Fig. C1.** The variation of the storage modulus $E^{'}$, and the loss modulus$\tan(\delta)$ with temperature (Baniasadi et al., 2021).

## References

Abbasi-Shirsavar, M., Baghani, M., Taghavimehr, M., Golzar, M., Nikzad, M., Ansari, M., George, D., 2019. An experimental-numerical study on shape memory behavior of PU/PCL/ZnO ternary blend. J. Intell. Mater. Syst. Struct. 30 (1), 116–126.

Abdolahi, J., Baghani, M., Arbabi, N., Mazaheri, H., 2017. Finite bending of a temperature-sensitive hydrogel tri-layer: an analytical and finite element analysis. Compos. Struct. 164, 219–228.

Abou-Ali, A.M., Al-Ketan, O., Rowshan, R., Al-Rub, R.A., 2019. Mechanical response of 3D printed bending-dominated ligament-based triply periodic cellular polymeric solids. J. Mater. Eng. Perform. 28 (4), 2316–2326.

Abueidda, D.W., Bakir, M., Al-Rub, R.K.A., Bergström, J.S., Sobh, N.A., Jasiuk, I., 2017. Mechanical properties of 3D printed polymeric cellular materials with triply periodic minimal surface architectures. Mater. Des. 122, 255–267.

Ahmadi, S., Hedayati, R., Li, Y., Lietaert, K., Tümer, N., Fatemi, A., Zadpoor, .A., 2018. Fatigue performance of additively manufactured meta-biomaterials: the effects of topology and material type. Acta Biomater. 65, 292–304.

Akbari, P., F. Ogoke, N.-Y. Kao, K. Meidani, C.-Y. Yeh, W. Lee, and A.B. Farimani, MeltpoolNet: Melt Pool Characteristic Prediction in Metal Additive Manufacturing Using Machine Learning. arXiv preprint arXiv:2201.11662, 2022.

Al-Ketan, O., Abu Al-Rub, R.K., 2019. Multifunctional mechanical metamaterials based on triply periodic minimal surface lattices. Adv. Eng. Mater. 21 (10), 1900524.

Alimov, M.M., Bazilevsky, A.V., Kornev, K.G., 2021. Soap film on two noncircular frames. Phys. Fluids 33 (5), 052104.

Arrieta, S., Diani, J., Gilormini, P., 2014. Experimental characterization and thermoviscoelastic modeling of strain and stress recoveries of an amorphous polymer network. Mech. Mater. 68, 95–103.

Asadzadeh, H., Moosavi, A., Arghavani, J., 2020. The effect of chitosan and PEG polymers on stabilization of GF-17 structure: a molecular dynamics study. Carbohydr. Polym. 237, 116124.

Baghani, M., Naghdabadi, R., Arghavani, J., 2012. A semi-analytical study on helical springs made of shape memory polymer. Smart Mater. Struct. 21 (4), 045014.

Baniasadi, M., Fareghi, P., Darijani, F., Baghani, M., 2020. Finite strain relaxation and creep in coupled axial and torsional deformation. Mech. Base. Des. Struct. Mach. 1–17. https://doi.org/10.1080/15397734.2020.1785311.

Baniasadi, M., Yarali, E., Foyouzat, A., Baghani, M., 2021. Crack self-healing of thermo-responsive shape memory polymers with application to control valves, filtration, and drug delivery capsule. Eur. J. Mech. Solid. 85, 104093.

Bayat, M.R., Dolatabadi, R., Baghani, M., 2020. Transient swelling response of pH-sensitive hydrogels: a monophasic constitutive model and numerical implementation. Int. J. Pharm. 577 https://doi.org/10.1016/j.ijpharm.2020.119030.

Blanquer, S.B., Werner, M., Hannula, M., Sharifi, S., Lajoinie, G.P., Eglin, D., Grijpma, .D. W., 2017. Surface curvature in triply-periodic minimal surface architectures as a distinct design parameter in preparing advanced tissue engineering scaffolds. Biofabrication 9 (2), 025001.

Bobbert, F., Lietaert, K., Eftekhari, A., Pouran, B., Ahmadi, S., Weinans, H., Zadpoor, A., 2017. Additively manufactured metallic porous biomaterials based on minimal surfaces: a unique combination of topological, mechanical, and mass transport properties. Acta Biomater. 53, 572–584.

Brinson, H.F., Brinson, L.C., 2008. Polymer Engineering Science and Viscoelasticity, vol. 66. Springer, New York, p. 79.

Cvijović, D., Klinowski, J., 1994. The computation of the triply periodic I-WP minimal surface. Chem. Phys. Lett. 226 (1–2), 93–99.

Damanpack, A., Aghdam, M., Shakeri, M., 2015. Micro-mechanics of composite with SMA fibers embedded in metallic/polymeric matrix under off-axial loadings. Eur. J. Mech. Solid. 49, 467–480.

Diani, J., Gilormini, P., Frédy, C., Rousseau, I., 2012. Predicting thermal shape memory of crosslinked polymer networks from linear viscoelasticity. Int. J. Solid Struct. 49 (5), 793–799.

Dietsch, B., Tong, T., 2007. A review-: features and benefits of shape memory polymers (smps). J. Adv. Mater. 39 (2), 3–12.

du Plessis, A., Razavi, S., Berto, F., 2020. The effects of microporosity in struts of gyroid lattice structures produced by laser powder bed fusion. Mater. Des. 194, 108899.

Gall, K., Yakacki, C.M., Liu, Y., Shandas, R., Willett, N., Anseth, K.S., 2005. Thermomechanics of the shape memory effect in polymers for biomedical applications. J. Biomed. Mater. Res. Part A: An Official Journal of The Society for Biomaterials 73 (3), 339–348. The Japanese Society for Biomaterials, and The Australian Society for Biomaterials and the Korean Society for Biomaterials.

Ghaderi, A., Morovati, V., Dargazany, R., 2020. A physics-informed assembly of feed-forward neural network engines to predict inelasticity in cross-linked polymers. Polymers 12 (11), 2628.

Gharehnazifam, Z., R. Dolatabadi, M. Baniassadi, H. Shahsavari, A.M. Kajbafzadeh, K. Abrinia, and M. Baghani, Computational analysis of vincristine loaded silk fibroin hydrogel for sustained drug delivery applications: multiphysics modeling and experiments. Int. J. Pharm., 609, 2021. doi: 10.1016/j.ijpharm.2021.121184.

Gharehnazifam, Z., Dolatabadi, R., Baniassadi, M., Shahsavari, H., Kajbafzadeh, A.-M., Abrinia, K., Baghani, .M., 2022. Multiphysics modeling and experiments on ultrasound-triggered drug delivery from silk fibroin hydrogel for Wilms tumor. Int. J. Pharm. 621, 121787 https://doi.org/10.1016/j.ijpharm.2022.121787.

Ghavidelnia, N., Bodaghi, M., Hedayati, R., 2020. Femur auxetic meta-implants with tuned micromotion distribution. Materials 14 (1), 114.

Gruskin, E., Doll, B.A., Futrell, F.W., Schmitz, J.P., Hollinger, J.O., 2012. Demineralized bone matrix in bone repair: history and use. Adv. Drug Deliv. Rev. 64 (12), 1063–1077.

Han, L., Che, S., 2018. An overview of materials with triply periodic minimal surfaces and related geometry: from biological structures to self-assembled systems. Adv. Mater. 30 (17), 1705708.

Hedayati, R., Sadighi, M., Mohammadi-Aghdam, M., Zadpoor, A., 2016. Mechanical properties of regular porous biomaterials made from truncated cube repeating unit cells: analytical solutions and computational models. Mater. Sci. Eng. C 60, 163–183.

Hedayati, R., Hosseini-Toudeshky, H., Sadighi, M., Mohammadi-Aghdam, M., Zadpoor, A., 2018. Multiscale modeling of fatigue crack propagation in additively manufactured porous biomaterials. Int. J. Fatig. 113, 416–427.

Hedayati, R., Roudbarian, N., Tahmasiyan, S., 2021. Using Gradient Origamis to Pre-program Curvatures. Engineering Archive.

Janbaz, S., Hedayati, R., Zadpoor, A., 2016. Programming the shape-shifting of flat soft matter: from self-rolling/self-twisting materials to self-folding origami. Mater. Horiz. 3 (6), 536–547.

Jebellat, E., Baniassadi, M., Moshki, A., Wang, K., Baghani, M., 2020. Numerical investigation of smart auxetic three-dimensional meta-structures based on shape memory polymers via topology optimization. J. Intell. Mater. Syst. Struct. 31 (15), 1838–1852. https://doi.org/10.1177/1045389x20935569.

Jebellat, I., Pishkenari, H.N., Jebellat, E., 2021. Training Microrobots via Reinforcement Learning and a Novel Coding Method. In: 2021 9th RSI International Conference on Robotics and Mechatronics (ICRoM).

Jin, B., Song, H., Jiang, R., Song, J., Zhao, Q., Xie, T., 2018. Programming a crystalline shape memory polymer network with thermo-and photo-reversible bonds toward a single-component soft robot. Sci. Adv. 4 (1), eaao3865.

Jung, Y., Torquato, S., 2005. Fluid permeabilities of triply periodic minimal surfaces. Phys. Rev. 72 (5), 056319.

Karageorgiou, V., Kaplan, D., 2005. Porosity of 3D biomaterial scaffolds and osteogenesis. Biomaterials 26 (27), 5474–5491.

Ko, Y.H., Razmjooei, N., Hemmati, H., Magnusson, R., 2021. Perfectly-reflecting guided-mode-resonant photonic lattices possessing Mie modal memory. Opt Express 29 (17), 26971–26982.

Kolken, H.M., Zadpoor, A., 2017. Auxetic mechanical metamaterials. RSC Adv. 7 (9), 5111–5129.

Lai, M., Kulak, A.N., Law, D., Zhang, Z., Meldrum, F.C., Riley, D.J., 2007. Profiting from nature: macroporous copper with superior mechanical properties. Chem. Commun. (34), 3547–3549.

Lendlein, A., Langer, R., 2002. Biodegradable, elastic shape-memory polymers for potential biomedical applications. Science 296 (5573), 1673–1676.

Liu, X.-N., Hu, G.-K., Huang, G.-L., Sun, C.-T., 2011. An elastic metamaterial with simultaneously negative mass density and bulk modulus. Appl. Phys. Lett. 98 (25), 251907.

Liu, Y., Du, H., Liu, L., Leng, J., 2014. Shape memory polymers and their composites in aerospace applications: a review. Smart Mater. Struct. 23 (2), 023001.

Lotfolahpour, A., Zaeem, M.A., 2021. Effects of cleavage plane and material strength on fracture of polycrystalline brittle materials: a phase-field modeling study. Comput. Mater. Sci. 197, 110642.

Mackay, A.L., 1985. Periodic minimal surfaces. Phys. B+C 131 (1–3), 300–305.

Magnusson, R., Ko, Y.H., Razmjooei, N., Simlan, F.A., Hemmati, H., 2022. Resonance properties of isolated-particle optical lattices: antireflection-quenched Mie scattering and Mie modal memory. In: Photonic and Phononic Properties of Engineered Nanostructures XII. SPIE.

Maszybrocka, J., Gapiński, B., Dworak, M., Skrabalak, G., Stwora, A., 2019. The manufacturability and compression properties of the Schwarz Diamond type Ti6Al4V cellular lattice fabricated by selective laser melting. Int. J. Adv. Manuf. Technol. 105 (7–8), 3411–3425.

Matsen, M.W., Bates, F.S., 1996. Unifying weak-and strong-segregation block copolymer theories. Macromolecules 29 (4), 1091–1098.

Michielsen, K., Kole, J., 2003. Photonic band gaps in materials with triply periodic surfaces and related tubular structures. Phys. Rev. B 68 (11), 115107.

Mohammadi, K., Movahhedy, M., Shishkovsky, I., Hedayati, R., 2020. Hybrid anisotropic pentamode mechanical metamaterial produced by additive manufacturing technique. Appl. Phys. Lett. 117 (6), 061901 https://doi.org/10.1063/5.0014167.

Moshki, A., Hajighasemi, M.R., Atai, A.A., Jebellat, E., Ghazavizadeh, A., 2022. Optimal design of 3D architected porous/nonporous microstructures of multifunctional multiphase composites for maximized thermomechanical properties. Comput. Mech. 69 (4), 979–996. https://doi.org/10.1007/s00466-021-02125-y.

Noroozi, R., Bodaghi, M., Jafari, H., Zolfagharian, A., Fotouhi, M., 2020. Shape-adaptive metastructures with variable bandgap regions by 4D printing. Polymers 12 (3), 519.

Poniznik, Z., Salit, V., Basista, M., Gross, D., 2008. Effective elastic properties of interpenetrating phase composites. Comput. Mater. Sci. 44 (2), 813–820.

Pouya, C., Overvelde, J.T., Kolle, M., Aizenberg, J., Bertoldi, K., Weaver, J.C., Vukusic, P., 2016. Characterization of a mechanically tunable gyroid photonic crystal inspired by the butterfly parides sesostris. Adv. Opt. Mater. 4 (1), 99–105.

Ptochos, E., Labeas, G., 2012. Elastic modulus and Poisson's ratio determination of micro-lattice cellular structures by analytical, numerical and homogenisation methods. J. Sandw. Struct. Mater. 14 (5), 597–626.

Qi, D., Yu, H., Liu, M., Huang, H., Xu, S., Xia, Y., Wu, .W., 2019. Mechanical behaviors of SLM additive manufactured octet-truss and truncated-octahedron lattice structures with uniform and taper beams. Int. J. Mech. Sci. 163, 105091.

Roudbarian, N., Baghani, M., Baniasadi, M., George, D., Mohammadi, A., 2019a. An experimental investigation on the energy storage in a shape-memory-polymer system. Energy Equip. Syst. 7 (4), 309–316.

Roudbarian, N., Baniasadi, M., Ansari, M., Baghani, M., 2019b. An experimental investigation on structural design of shape memory polymers. Smart Mater. Struct. 28 (9), 095017.

Roudbarian, N., Baniasadi, M., Nayyeri, P., Ansari, M., Hedayati, R., Baghani, M., 2021. Enhancing shape memory properties of multi-layered and multi-material polymer composites in 4D printing. Smart Mater. Struct. 30 (10), 105006 https://doi.org/10.1088/1361-665x/ac1b3b.

Sadipour, M., Hanafizadeh, P., Sadeghy, K., Sattari, A., 2020. Effect of aortic wall deformation with healthy and calcified annulus on hemodynamic performance of implanted on-X valve. Cardiovascular Eng. Technol. 11 (2), 141–161.

Safranski, D.L., Gall, K., 2008. Effect of chemical structure and crosslinking density on the thermo-mechanical properties and toughness of (meth) acrylate shape memory polymer networks. Polymer 49 (20), 4446–4455.

Sathishkumar, N., Vivekanandan, N., Balamurugan, L., Arunkumar, N., Ahamed, I., 2020. Mechanical properties of triply periodic minimal surface based lattices made by polyjet printing. Mater. Today Proc. 22, 2934–2940.

Schoen, A.H., 1970. Infinite Periodic Minimal Surfaces without Self-Intersections. National Aeronautics and Space Administration.

Schwarz, H.A., 1890. Gesammelte Mathematische Abhandlungen, vol. 1. J. Springer.

Shalaev, V.M., 2007. Optical negative-index metamaterials. Nat. Photonics 1 (1), 41–48.

Smith, D.R., Pendry, J.B., Wiltshire, M.C., 2004. Metamaterials and negative refractive index. Science 305 (5685), 788–792.

Soyarslan, C., Blümer, V., Bargmann, S., 2019. Tunable auxeticity and elastomechanical symmetry in a class of very low density core-shell cubic crystals. Acta Mater. 177, 280–292.

Spicer, P.P., Kretlow, J.D., Young, S., Jansen, J.A., Kasper, F.K., Mikos, A.G., 2012. Evaluation of bone regeneration using the rat critical size calvarial defect. Nat. Protoc. 7 (10), 1918–1929.

Udhayaraman, R., Mulay, S.S., 2019. Multi-scale damage framework for textile composites: application to plain woven composite. Eur. J. Mech. Solid. 77, 103809.

Ward Small, I., Singhal, P., Wilson, T.S., Maitland, D.J., 2010. Biomedical applications of thermally activated shape memory polymers. J. Mater. Chem. 20 (17), 3356–3366.

Westbrook, K.K., Kao, P.H., Castro, F., Ding, Y., Qi, H.J., 2011. A 3D finite deformation constitutive model for amorphous shape memory polymers: a multi-branch modeling approach for nonequilibrium relaxation processes. Mech. Mater. 43 (12), 853–869.

Xie, R., Hu, J., Hoffmann, O., Zhang, Y., Ng, F., Qin, T., Guo, X., 2018. Self-fitting shape memory polymer foam inducing bone regeneration: a rabbit femoral defect study. Biochim. Biophys. Acta Gen. Subj. 1862 (4), 936–945.

Yakacki, C.M., Shandas, R., Lanning, C., Rech, B., Eckstein, A., Gall, K., 2007. Unconstrained recovery characterization of shape-memory polymer networks for cardiovascular applications. Biomaterials 28 (14), 2255–2263. https://doi.org/10.1016/j.biomaterials.2007.01.030.

Yang, C., Boorugu, M., Dopp, A., Ren, J., Martin, R., Han, D., Lee, .H., 2019. 4D printing reconfigurable, deployable and mechanically tunable metamaterials. Mater. Horiz. 6 (6), 1244–1250.

Yarali, E., Taheri, A., Baghani, M., 2020a. A comprehensive review on thermomechanical constitutive models for shape memory polymers. J. Intell. Mater. Syst. Struct. 1045389X20916795.

Yarali, E., Noroozi, R., Moallemi, A., Taheri, A., Baghani, M., 2020b. Developing an analytical solution for a thermally tunable soft actuator under finite bending. Mech. Base. Des. Struct. Mach. 1–15. https://doi.org/10.1080/15397734.2020.1763182.

Yin, H., Zheng, X., Wen, G., Zhang, C., Wu, Z., 2021. Design optimization of a novel bio-inspired 3D porous structure for crashworthiness. Compos. Struct. 255, 112897.

Zadpoor, A.A., 2016. Mechanical meta-materials. Mater. Horiz. 3 (5), 371–381.

Zhang, W., Zhang, F., Lan, X., Leng, J., Wu, A.S., Bryson, T.M., Chou, .T.-W., 2018. Shape memory behavior and recovery force of 4D printed textile functional composites. Compos. Sci. Technol. 160, 224–230.

Zhao, W., Liu, L., Zhang, F., Leng, J., Liu, Y., 2019. Shape memory polymers and their composites in biomedical applications. Mater. Sci. Eng. C 97, 864–883.